A NUMERICAL SIMULATION OF BOUNDARY-LAYER FLOWS NEAR SHELTERBELTS

HAO WANG* and EUGENE S. TAKLE
Department of Geological and Atmospheric Sciences, and Department of Agronomy, Iowa State University, Ames, Iowa 50011, USA

(Received in final form 5 January, 1995)

Abstract. We have developed a shelterbelt boundary-layer numerical model to study the patterns and dynamic processes relating to flow interaction with shelterbelts. The model simulates characteristics of all three zones of airflow passing over and through shelterbelts: the windward windspeed-reduction zone, the overspeeding zone above the shelterbelt, and the leeward windspeed- reduction zone. Locations of the maximum windspeed reduction and recirculation zone, as well as the leeward windspeed-recovery rate are well simulated by the model. Where comparisons with field measurements and wind-tunnel experiments were possible, the model demonstrated good performance for flows over and through shelters ranging from almost completely open to almost solid.

The dynamic pressure resulting from the convergence and divergence of the flow field alters the perturbation pressure field. The disturbed pressure controls not only the formation of the separated flow but also the location of maximum windspeed reduction, streamline curvature, speed-up over the shelterbelt, and leeward windspeed recovery rate. The interaction of pressure with the flow produces complex flow patterns, the characteristics of which are determined, to a great extent, by shelterbelt structure.

1. Notation

$\langle\ \rangle$	Spatial averaged value
$(\bar{})$	Temporal averaged value
$(')$	Departure of variable from its averaged value
A	Leaf surface-area density
ABL	Atmospheric boundary layer
C	Drag coefficient for obstacle exerted on air
C_d	Drag coefficient for unit plant area density
c_i	Experimental constants of turbulent closure scheme (Mellor and Yamada, 1982)
E	Turbulent kinetic energy (TKE)
F_i	Drag force in the i direction exerted on air flow by obstacle elements
f_k	Coriolis parameter
g_i	Acceleration vector due to gravity
H	Height of shelterbelt
i, j, k, q	Subscript variables, indicating x, y and z directions, respectively, and grid numbers in these three directions
K_0	Turbulent exchange coefficient for neutral, obstacle-free ABL

* *Corresponding author:* Dr. Hao Wang, Department of Geological and Atmospheric Sciences, Iowa State University, 3010 Agronomy Hall, Ames, Iowa 50011, U.S.A.

Boundary-Layer Meteorology **75:** 141–173, 1995.

K_m	Turbulent exchange coefficient for momentum transport
K_E	Turbulent exchange coefficient for TKE transport
k_r	Resistance coefficient of shelterbelts
l	Mixing length of turbulence
MKE	Mean kinetic energy
n	Timestep of model integration
$\mathbf{n}$, n_i	Vector and its component in the i direction of the interface of the averaging volume
p	Atmospheric pressure perturbation
S	Interface surface of the averaging volume
t	Time
U	Total mean windspeed
u, w	Mean windspeed components in x and z directions, respectively
u', w'	Fluctuating windspeed components in x and z directions
u_i	Windspeed in the i direction
u_*	Friction velocity
u_{*0}	Friction velocity for obstacle-free ABL
u_t, v_t	u and v at model top
u^{aux}, and w^{aux}	Intermediate prediction velocities of u and w without the dynamic pressure perturbation
u^{n+1} and w^{n+1}	Prediction velocities of u and w at the $n+1$ timestep of model integration
V	Volume of the spatial averaging process
x	Horizontal coordinate axis perpendicular to shelterbelt
x_i	$i = 1, 2, 3$ – three direction coordinate, x, y, z
z	Vertical coordinate axis upward
z_0	Ground surface roughness length
β	Weight coefficient for numerical differencing scheme
γ	Coefficient of air thermal expansion
ϵ	Dissipation rate of turbulence
ϵ_{ijk}	Einstein summation symbol
ρ_0	Air density
θ	Potential-temperature departure from its basic state
ν	Coefficient of air molecular viscosity
Δt	Time step of model integration
κ	von Karman constant
ϕ	Macro symbol, standing for u, v, w, E and $E1$

2. Introduction

The primary effect of any shelterbelt or windbreak system is the reduction in wind velocity. Windspeed reduction influences turbulent transport processes and modifies the microclimate in the sheltered zone. The amount of sheltering and the range of the sheltered zone are dependent on the structure of shelterbelt. Experimental

studies of the last 30 years have been carried out to measure windspeed and turbulence, both in the laboratory with wind-tunnel models and at full scale in the field. Numerous papers on interpretation of empirical data have been published, and several review papers are available (e.g. van Eimern, 1964; Rosenberg, 1979; McNaughton, 1988; Heisler and Dewalle, 1988). Development of a detailed basic understanding of the flow field is a complex analytical and numerical problem since a complete treatment requires a solution of the full turbulent Navier-Stokes equations. It is not surprising then that most shelterbelt research has been experimental, emphasizing windspeed reduction produced by shelterbelts. A full understanding of shelterbelt aerodynamics is not available, even for the relatively simple artificial linear barrier of uniform porosity resting on a uniform surface of infinite extent.

Theoretical and numerical modeling research on shelterbelts has been reported by Kaiser (1959), Plate (1971), Counihan *et al.* (1974), Taylor (1988), Hagen *et al.* (1981) and Wilson (1985). Analytic solutions are somewhat easier to obtain for the far wake region ($x > 10$ H), well downstream of the obstacle itself; but for the region in which the protection is greatest ($x < 10$ H), the streamline shape becomes important, and quantitative results become rather complex and difficult to obtain analytically. Kaiser (1959) obtained an error-function formula by assuming that the momentum deficit in the sheltered region is replenished by diffusion of a passive scalar. This model does not have sufficient physics to describe complex turbulent flow interactions and cannot be expected to predict the location of maximum wind reduction.

Wilson (1985) used several well-known turbulent closure models ranging from a simple upstream $K_0 = ku_{*0}z$ to $K - E$ closure, $K - E - \epsilon$ closure, and second-order closure schemes to compare patterns of flow through a porous windbreak. He reported that all turbulence schemes gave satisfactory agreement with the observed velocity deficit in the near wake region of the fence but that speed-up over the fence and leeward windspeed recovery rates for all simulations were less than observed. He concluded that the models' failure to predict the correct windspeed recovery rate in the lee of a fence was a consequence of the models' failure to capture the overspeeding over the fence. Correction of streamline curvature by modifying the turbulence did not give completely satisfactory results for either overspeeding or the recovery rate.

Most past research considered the sheltering effect to be described by a form-drag force which produced a windspeed deficit immediately behind the shelterbelt and that this windspeed deficit is diffused downwind by turbulence to produce the leeward windspeed reduction. The classical interpretation of the dependence of horizontal sheltering distance on shelterbelt porosity is as follows: very dense shelterbelts cause a strong speed reduction immediately behind the belt and create more downwind turbulence than medium-dense shelterbelts. The higher turbulence may result in rapid recovery of mean horizontal windspeeds to upwind values at locations much closer to low-porosity shelterbelts, thus resulting in a much shorter protected distance (van Eimern *et al.*, 1964). Contrary to this classical interpreta-

tion, measurements with tree windbreaks (Sturrock, 1969, 1972; Caborn, 1957), artificial barriers (Hagen and Skidmore, 1971) or in wind tunnels (Jensen, 1974; Raine and Stevenson, 1977) show that there is only slight fall-off of the sheltering horizontal distance for dense trees and solid fences, far smaller than the fall-off suggested by Naegeli (cited by van Eimern *et al.*, 1964). Wilson (1985) reasoned that the TKE generated near windbreaks is at small scales, which dissipates rapidly and contributes little to transport of momentum.

In summary, we concluded that there is need for a model that simulates effects of the shelter with sufficient detail to accurately simulate (1) speed-up over a shelter, (2) recovery rate of windspeed in the lee, and (3) recirculating flows behind very dense shelters. Such a model should then resolve the present disagreement on the relation of porosity to sheltering effect. We have developed a shelterbelt boundary-layer turbulence model for studying the aerodynamics of shelterbelts and their dependence on shelterbelt porosity expressed by leaf-area-index (LAI) density, i.e., the leaf area per unit volume. This model enables us to analyze characteristics of the sheltering effect, both upwind and downwind, in sufficient detail to resolve many questions about the processes governing the aerodynamics of porous shelters.

3. Model

3.1. Equations

Under the Boussinesq approximation, the non-hydrostatic, incompressible atmospheric continuity equation and equations of motion may be written as

$$\frac{\partial u_i}{\partial x_i} = 0, \tag{1}$$

$$\frac{\partial u_i}{\partial t} = -u_j \frac{\partial u_i}{\partial x_j} - \frac{1}{\rho_0}\frac{\partial p}{\partial x_i} - \gamma g_i \theta - \epsilon_{ijk} f_k u_j + \nu \frac{\partial^2 u_i}{\partial x_i^2}, \tag{2}$$

where the Einstein summation is used. We use the conventional definitions of mean and turbulent variables and Reynolds averaging.

3.2. Parameterization of shelterbelts

All physical variables, such as windspeed, pressure, temperature, and turbulent variables and the equations for mean and turbulent properties are defined in the interstitial air space within the porous obstacle but have no meaning in the space occupied by solid elements. These solid elements of the shelterbelt act as interior boundaries within the ABL flow. Therefore, we are faced with very complex boundary conditions to properly treat the flow problem in porous shelterbelts.

Only for two-dimensional artificial barriers with simple geometric shapes (such as a fence or plane having circular holes) is it possible to treat the details of the barrier boundaries to the flow. For natural tree shelterbelts and most artificial shelterbelts, the boundaries of the solid elements are too complex and irregular to be treated explicitly. On the other hand, it is unnecessary to treat all details of solid element boundaries, because the purpose of shelterbelt research is to describe the flow in the protected zone outside the shelterbelt rather than in the shelterbelt itself. Our research focuses on flow patterns near shelterbelts, such as the leeward wake flow and overspeeding over the top of the shelterbelt. Therefore, we can neglect the detailed structure of the complex solid boundaries within shelterbelts and consider them as an aggregate effect, described by a form-drag force on the airflow penetrating the shelter.

We are next faced with choice of a method for averaging Equations (1), (2), and the turbulence equations that result from them. Wilson and Shaw (1977) first developed a large plane averaging method to include canopy effects in their canopy flow model. Later Raupach and Shaw (1982) and Finnigan (1985) presented time/horizontal-plane and time/volume averaging schemes. Several investigators used these methods to successfully simulate forest and crop flows (Yamada, 1982; Wilson and Shaw, 1977; Wilson, 1985, 1987, 1988; Meyers and Paw U, 1986; Naot and Mahrer, 1991; Li *et al.*, 1989; Miller *et al.*, 1991).

We subject the equations to phase averaging (Whitaker, 1968, 1969, 1973; Wang and Takle, 1995), which requires an assumption that the solid elements are motionless. The spatial averaging length scale is both small relative to length scales of mean variation and large relative to the element dimensions of shelterbelts. This averaging process produces surface integrals over the complex boundaries of the obstacles that add extra terms to the mean and turbulence equations (Wang and Takle, 1995). The continuity equation, equations of mean motion, and Reynolds-stress equations, after being subjected to this averaging process, are as follows

$$\frac{\partial \overline{\langle u_i \rangle}}{\partial x_i} = 0, \tag{3}$$

$$\begin{aligned} \frac{\partial \overline{\langle u_i \rangle}}{\partial t} = & -\overline{\langle u_j \rangle} \frac{\partial \overline{\langle u_i \rangle}}{\partial x_j} - \frac{\partial (\overline{\langle u_i \rangle' \langle u_j \rangle'})}{\partial x_j} - \epsilon_{ijk} f_k \overline{\langle u_j \rangle} \\ & -\gamma g_i \overline{\langle \theta \rangle} - \frac{1}{\rho_0} \frac{\partial \overline{\langle p \rangle}}{\partial x_i} + \nu \frac{\partial^2 \overline{\langle u_i \rangle}}{\partial x_j^2} - \frac{1}{\rho_0} F_i, \end{aligned} \tag{4}$$

and

$$\frac{\partial \overline{\langle u_i \rangle' \langle u_j \rangle'}}{\partial t} = -\overline{\langle u_k \rangle} \frac{\partial \overline{\langle u_i \rangle' \langle u_j \rangle'}}{\partial x_k} - \overline{\langle u_i \rangle' \langle u_k \rangle'} \frac{\partial \overline{\langle u_j \rangle}}{\partial x_k} -$$

$$
\begin{aligned}
&-\overline{\langle u_j\rangle'\langle u_k\rangle'}\frac{\partial\overline{\langle u_i\rangle}}{\partial x_k} - \gamma(g_i\overline{\langle u_j\rangle'\langle\theta\rangle'} + g_j\overline{\langle u_i\rangle'\langle\theta\rangle'}) - \\
&-f_k(\epsilon_{jkq}\overline{\langle u_i\rangle'\langle u_q\rangle'} + \epsilon_{ikq}\overline{\langle u_j\rangle'\langle u_q\rangle'}) - \\
&-\frac{\partial\overline{\langle u_k\rangle'\langle u_i\rangle'\langle u_j\rangle'}}{\partial x_k} - \frac{1}{\rho_0}\left(\frac{\partial\overline{\langle u_i\rangle'\langle p\rangle'}}{\partial x_j} + \frac{\partial\overline{\langle u_j\rangle'\langle p\rangle'}}{\partial x_i}\right) + \\
&+\frac{1}{\rho_0}\overline{\langle p\rangle'\left(\frac{\partial\langle u_i\rangle'}{\partial x_j} + \frac{\partial\langle u_j\rangle'}{\partial x_i}\right)} + \nu\frac{\partial^2\overline{\langle u_i\rangle'\langle u_j\rangle'}}{\partial x_k^2} - \\
&-2\nu\overline{\frac{\partial\langle u_i\rangle'}{\partial x_k}\frac{\partial\langle u_j\rangle'}{\partial x_k}} + \frac{1}{\rho_0}\overline{\langle u_i\rangle}F_j + \frac{1}{\rho_0}\overline{\langle u_j\rangle}F_i, \qquad (5)
\end{aligned}
$$

where the overline of variables stands for the time average of the variables, prime stands for fluctuation from the time average, and angle brackets around a term or variable indicate the spatial average. Following all previous investigators, the dispersive terms are assumed negligible.

Compared to equations for the obstacle-free ABL, the continuity equation has the same form, but the equations of mean motion have additional terms arising from the form drag caused by the obstacle elements. The Reynolds-stress equations have two additional terms related to this force. This force can be expressed as

$$
F_i = \overline{\frac{1}{V}\int_S\int pn_i\,\mathrm{d}S'} - \overline{\frac{\nu}{V}\int_S\int\frac{\partial u_i}{\partial\mathbf{n}}\,\mathrm{d}S'}. \qquad (6)
$$

This is the sum of the integration of pressure and wind shear over the obstacle elements' surface area (S) within averaging volume (V), where $\mathbf{n}$ is a unit normal vector outward from S and n_i is its component in the i direction. This force represents momentum sinks of (pressure) form drag (which is by far the larger of the two) and viscous skin-friction drag on the mean flow by the plant canopy elements. Following Thom (1975), the drag force per unit surface area may be expressed by the commonly used formula

$$
F_i = \rho_0 C U u_i, \qquad (7)
$$

where C is a drag coefficient for an obstacle element, and U is the mean windspeed defined as

$$
U = \sqrt{\langle u_i\rangle\langle u_i\rangle}. \qquad (8)
$$

For the vegetation case, formula (7) can be rewritten as

$$
F_i = \rho_0 C_d A U u_i, \qquad (9)
$$

where C_d is a drag coefficient for unit leaf-area density, A, which is the leaf-area index divided by the height of the shelter. For convenience, hereafter we shall omit angle brackets and overlines over mean variables.

3.3. SIMPLIFICATION AND TURBULENT CLOSURE

For simplicity let us consider the equations of motion for neutral stratification. A typical shelterbelt height of about 10 m is much less than the height of the ABL, so the effect of Coriolis forces may be neglected. Shelterbelts are generally planted in rows perpendicular to the prevailing wind direction, and their length is at least one order larger than their height. Therefore we can consider a 2-D computational domain (vertical and horizontal along the wind perpendicular to the shelterbelt), for which the basic equations of motion and continuity equation may be simplified as

$$\frac{\partial u}{\partial t} = -\frac{1}{\rho_0}\frac{\partial p}{\partial x} - u\frac{\partial u}{\partial x} - w\frac{\partial u}{\partial z} - \frac{\partial \overline{u'^2}}{\partial x} - \frac{\partial \overline{u'w'}}{\partial z} - C_d A U u, \tag{10}$$

$$\frac{\partial w}{\partial t} = -\frac{1}{\rho_0}\frac{\partial p}{\partial z} - u\frac{\partial w}{\partial x} - w\frac{\partial w}{\partial z} - \frac{\partial \overline{u'w'}}{\partial x} - \frac{\partial \overline{w'^2}}{\partial z} - C_d A U w, \tag{11}$$

$$\frac{\partial u}{\partial x} + \frac{\partial w}{\partial z} = 0. \tag{12}$$

Equations (10) and (11) of mean motion include turbulent stress terms for which we must apply a boundary-layer turbulence-closure scheme. We tested the sensitivity to a hierarchy of second-order closure schemes proposed by Mellor and Yamada (Mellor and Yamada, 1974, 1882; Yamada and Mellor, 1975; Yamada, 1982), which are widely used in atmospheric sciences. Our results are consistent with Wilson's (1985) findings. For this paper, we select the simplified second-order turbulent closure scheme which Yamada (1982) used to model turbulent airflow in and above a forest canopy. We select this scheme for three reasons: (1) it provides a better physical basis than simple K schemes, (2) it is computationally efficient, and (3) it may be used to model the crop environment in the sheltered zones of shelterbelts in future applications. The $K - E - l$ scheme that we have chosen is somewhat like a two-equation $K - E - \epsilon$ scheme. The sensitivity tests showed that both schemes give nearly the same results for mean flows.

In Equations (10) and (11), the velocity fluctuation correlations (Reynolds stress) terms may be expressed as

$$-\overline{u_i' u_j'} = K_m \left(\frac{\partial u_i}{\partial x_j} + \frac{\partial u_j}{\partial x_i} \right) - \frac{2}{3} E \delta_{ij}, \tag{13}$$

$$K_m = c_1 l E^{1/2}. \tag{14}$$

With the above simplifications, Equation (5) gives the TKE equation as

$$\frac{\partial E}{\partial t} = -u\frac{\partial E}{\partial x} - w\frac{\partial E}{\partial z} + \frac{\partial}{\partial x_i}\left(K_E\frac{\partial E}{\partial x_i}\right) - \overline{-u_i'u_j'}\frac{\partial u_i}{\partial x_j} - c_2\frac{E^{3/2}}{l} + C_dAU^3. \quad (15)$$

Following Yamada (1982), the mixing length, l, can be predicted as

$$\frac{\partial El}{\partial t} = -u\frac{\partial El}{\partial x} - w\frac{\partial El}{\partial z} + \frac{\partial}{\partial x_i}\left(K_E\frac{\partial El}{\partial x_i}\right) - c_3l\overline{-u_i'u_j'}\frac{\partial u_i}{\partial x_j} - c_4E^{3/2}\left[1 + c_5\left(\frac{l}{kz}\right)^2\right] + C_dAlU^3, \quad (16)$$

where c_1–c_5 are constants determined from laboratory experiments (Mellor and Yamada, 1982). The changes of these parameters under some restraint relationships (Mellor and Yamada, 1982) are not as sensitive to mean flow patterns of the shelterbelt as to turbulence.

3.4. Numerical aspects

3.4.1. *Computational domain and grid*

The model computational domain is from 30 H upstream to 50 H downstream of the shelterbelt in the streamwise direction and from the ground to 8 H in the vertical. The shelterbelt effect on airflow can be considered as a 2-D advection problem wherein the air encounters a very narrow surface inhomogeneity consisting of a vertically extended line of porous obstacles. All observations and our calculated results show that the windward maximum distance of perturbed flow is about 10 H, so we set the upstream boundary at 30 H. Our results showed no effect of the upstream boundary on flow near the shelterbelt. Two factors determine the selection of model height: omission of the Coriolis force restricts our computational domain to the lower part of the ABL; on the other hand, we should select a model top as high as possible so as to avoid the effect of the shelterbelt. In this paper, the domain height is 8 H. Previous experimental results and our results showed negligible effects of the shelterbelt at the model top when we use "open"-top boundary conditions. We divide the domain into 81 levels in the vertical with a constant interval of 0.1 H, and 161 grid points in the horizontal with a constant interval of 0.5 H. The test of sensitivity to horizontal interval shows no obvious differences in the simulated results between 0.1 and 0.5 H.

3.4.2. *Solution technique*

We solve a system of 5 equations including equations for horizontal motion (10), nonhydrostatic vertical motion (11), mass conservation (12), TKE (15), and mixing length (16) linked by formulae (13) and (14). We use the finite-difference

method to discretize these 5 equations into a set of algebraic equations with tri-diagonal matrices, with forward differencing for the time terms, centered differencing for pressure terms, and upstream differencing for advection terms. The modified Crank–Nicholson scheme is used for the turbulent flux terms (Paegle *et al.*, 1976). We use the Alternating Direction Implicit (ADI) method to solve these equations in both vertical and horizontal directions. Because they include dynamic pressure, the equations are of the mixed parabolic-elliptic type. The dynamic pressure perturbation gradients are dropped from the momentum equations, and a set of auxiliary velocity fields u^{aux} and w^{aux} are computed based on Chorin's (1968) scheme. The results are then substituted into primitive equations:

$$u^{n+1} = u^{\text{aux}} - \frac{\Delta t}{\rho_0}\frac{\partial p}{\partial x}, \tag{17}$$

$$w^{n+1} = w^{\text{aux}} - \frac{\Delta t}{\rho_0}\frac{\partial p}{\partial z}, \tag{18}$$

where Δt is timestep, u^{n+1} and w^{n+1} are predictions of u and w at the $n+1$ timestep. To calculate divergence, we use

$$\frac{\partial u^{n+1}}{\partial x} + \frac{\partial w^{n+1}}{\partial z} = \frac{\partial u^{\text{aux}}}{\partial x} + \frac{\partial w^{\text{aux}}}{\partial z} - \frac{\Delta t}{\rho_0}\left(\frac{\partial^2}{\partial x^2} + \frac{\partial^2}{\partial z^2}\right) p. \tag{19}$$

The auxiliary velocity fields do not necessarily satisfy the equation of continuity, but u^{n+1} and w^{n+1} are mass conserving. Therefore, Equation (19) becomes

$$\left(\frac{\partial^2}{\partial x^2} + \frac{\partial^2}{\partial z^2}\right)\frac{p}{\rho_0} = \left(\frac{\partial u^{\text{aux}}}{\partial x} + \frac{\partial w^{\text{aux}}}{\partial z}\right)/\Delta t. \tag{20}$$

This dynamic pressure equation is solved by the SOR method with a relaxation factor of 1.75 and a successive convergence criterion of $|\delta(p_{\max}/\rho_0)| < 10^{-4}$ m^2/s^2. After computing dynamic pressure, we can correct the velocity field by Equations (17) and (18) and obtain the $(n+1)$-step velocity field.

We use the time-dependent model to obtain a stationary solution. When we developed this model, we first examined the changes of predicted values with time under stationary forcing by integrating the model out to 60 hr. The mean kinetic energy (MKE) and TKE reached their stationary values after about 2 hr. We also found that the computational accuracy for dynamic pressure was the key condition for keeping the cumulative error small for long-time integrations. When we use double precision for dynamic pressure and a successive convergence criterion of 10^{-4} m^2/s^2, we controlled the model relative computational error to less than 10^{-3} and produced reliable stationary solutions. When the differences of TKE and MKE between successive 1 hr integrations were less than the control level (in this paper, 0.01%), the computed results were considered to be steady-state results.

3.5. Initial and boundary conditions

We first omit the shelterbelt, assume that the ground is horizontally homogeneous, and compute the initial wind, TKE and mixing-length profiles with a 1-D version of the present model under prescribed windspeed at the model top boundary. The resulting profile of windspeed is nearly logarithmic. These profiles are also used as inflow lateral boundary conditions. The initial vertical velocity, w, is set equal to zero.

At the outflow boundary, the normal derivatives of all physical variables (u, w, p, E and El) are set equal to zero.

At the top boundary:

$$K_m \frac{\partial u}{\partial z} = u_*^2; \qquad K_E \frac{\partial E}{\partial z} = 0; \qquad \frac{\partial p}{\partial z} = 0. \tag{21}$$

At the lower boundary, a no-slip condition is imposed for wind, i.e. $u = w = 0$, and

$$E = C_2^{-2/3} u_*^2; \qquad El = \kappa z_0 E; \qquad \frac{\partial p}{\partial z} = 0, \tag{22}$$

where z_0 is the surface roughness length, which may be determined by the conventional windspeed log-profile, and $u*$ is the friction velocity which is calculated with the model-predicted windspeed at the lowest level (Wilson, 1985). Tests of the effects of z_0/H on the flow showed that z_0/H had little effect on the flow patterns of the shelterbelt but had some effect on the windspeed recovery rate in the lee.

4. Results and Discussion

We begin an overview of shelter effects by analyzing the changes of flow patterns with shelterbelt density, paying close attention to the formation processes, to the characteristics of the separated recirculations, and to the location of maximum windspeed reduction. We simulate 36 shelterbelts ranging from nearly open to nearly solid ones. We use the drag coefficient to estimate porosity, which is our descriptor of shelterbelt structure. The resistance coefficients may be estimated as

$$k_r = \int_{-\infty}^{+\infty} C_d A \, \mathrm{d}x. \tag{23}$$

The relationship between porosity and k_r has been revealed by many tunnel experiments. Based on Figure 1 of Heisler and Dewalle (1988) and Hoerner's (1965)

formula, we estimate the porosities corresponding to form drag coefficients adopted in our simulations. We emphasize that porosity only represents the planar geometrical structure of the shelterbelt, but that changes in flow are more correctly described by dynamic, not geometrical, parameters. The resistance coefficient (k_r) is a dynamic parameter that depends not only on porosity but also on the shape of the barrier elements. Barriers of equal porosity may have different k_r and different shelter effects. As reviewed by Heisler and Dewalle (1988), Baines and Peterson (1951) reported a range in k_r from 1.0 for a lattice of round material to 3.2 for a square bar lattice for a constant porosity of 0.5, and Richards *et al.* (1984) found a somewhat larger range in k_r, from 1.5 for a screen of smooth round elements to 5.0 for flat, sharp-edged elements, also for a porosity of 0.5. Therefore, when we use porosity, we also give the resistance coefficient in parentheses.

Plots of flow patterns over the whole range of shelterbelt porosities given in Figure 1 provide an opportunity to understand the physical and dynamic processes of shelterbelt effects on air flow and to examine the entire range of shelter effects. We analyze these to determine the dependence of flow patterns on shelterbelt porosity.

We can divide the flow patterns into two regimes: I, unseparated flow (Figures 1a–1d, with porosities of 0.99–0.4); and II, separated flow (Figures 1e–1j, with porosities of 0.3–0.06). In regime I, streamline curvature increases with decreasing porosity. Figure 1a, which represents a nearly open-density case with a porosity of 0.99 (0.005), shows no obvious change in streamline curvature; for a porosity of 0.83 (0.125), streamlines at the top of the shelter show slight upward curvature from 3 H windward to 5 H leeward and then slope downward to the undisturbed flow (Figure 1b). This feature may be more clearly seen in Figure 1c for a porosity of 0.62 (0.5). When the porosity increases to 0.4 (2.0), the upward streamlines become steeper and streamline compression exists over the top of the shelterbelt. The streamlines show a slight downward curvature windward close to the ground surface near the shelterbelt.

The characteristics of separated flow (regime II) are important features of the physics and dynamics of shelterbelts, because the current differences of views about the relationship between shelter effects and shelterbelt density centers on this regime. Figure 1e shows the initial separating recirculation for a porosity of 0.30 (3.0). The separated recirculation is very weak and is located $x = 6$ H leeward of the shelterbelt. It separates at $x = 5$ H and reattaches at $x = 8$ H. The stagnation point is at $x = 6.5$ H and $z = 0.15$ H. Figures 1f–1j show results for successively more dense shelters. The center of the recirculation zone generally moves toward the shelter and up as the porosity decreases. The separation point moves to $x = 0$ H, and the reattachment point decreases to $x = 5$ H.

These features agree with available observations and smoke trace experiments, which show that dense shelterbelts with porosity less than 0.3 may produce a recirculation bubble in their lee (Heisler and Dewalle, 1988; Perera, 1981; Castro, 1971). The recirculation is rather weak, and the recirculation zone is very small

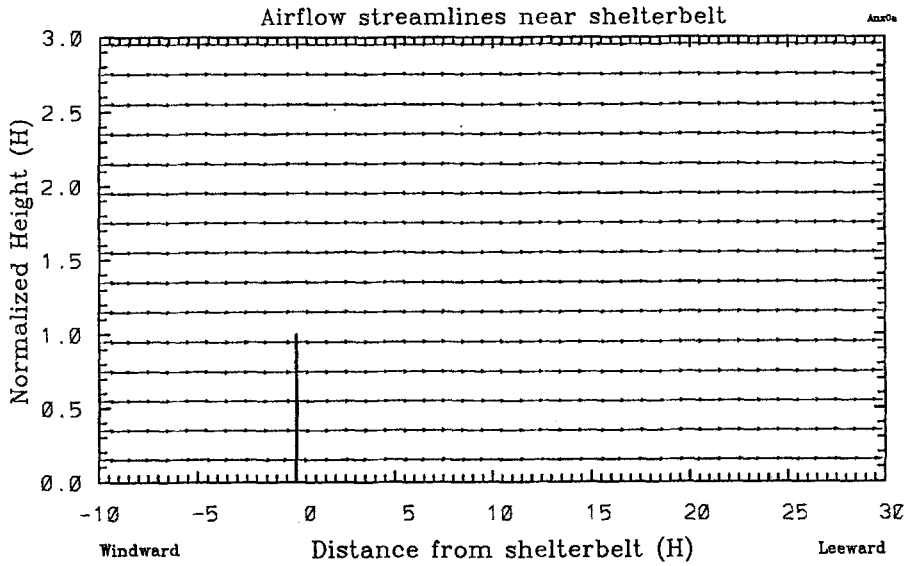

Fig. 1a. Streamline pattern of airflow through a shelterbelt with porosity of 0.99 (k_r = 0.005).

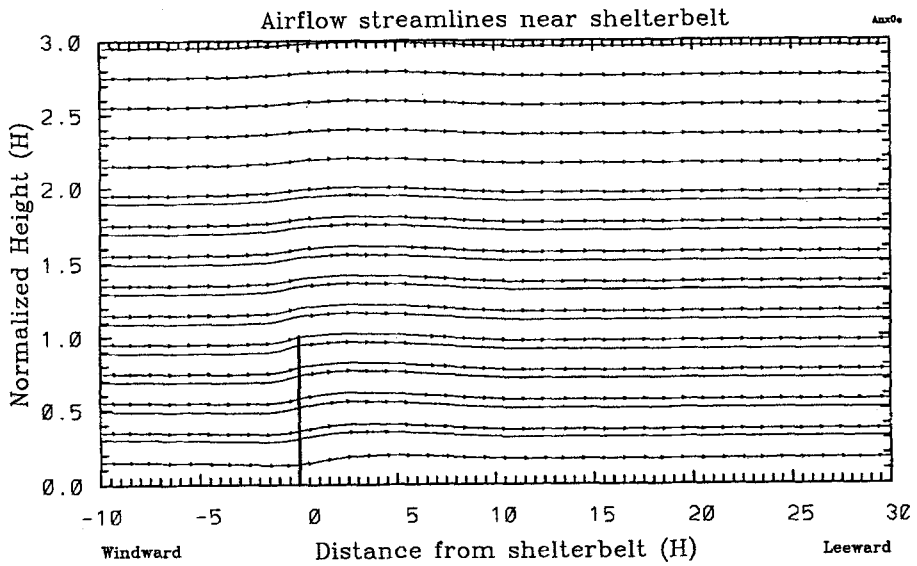

Fig. 1b. Same as Figure 1a but for a porosity of 0.83 (k_r = 0.125).

when it just begins to form at a critical porosity of 0.3. Even for a porosity of 0.27 (4.0), the simulated maximum reverse windspeed is still less than 0.5 m/s. Quantitative measurements are very difficult in highly distorted flows for small reverse windspeed. Therefore, small and weak recirculation far downstream very likely escapes observation.

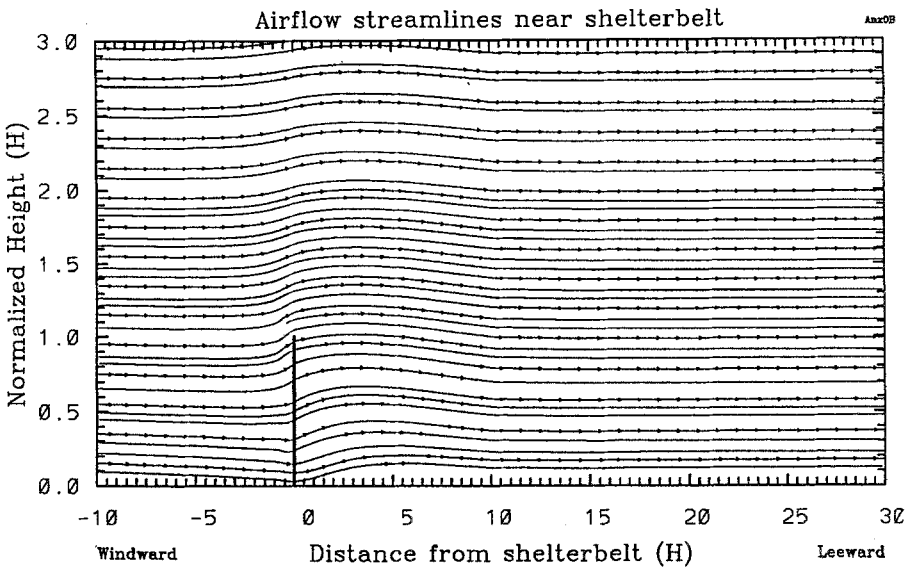

Fig. 1c. Same as Figure 1a but for a porosity of 0.62 ($k_r = 0.5$).

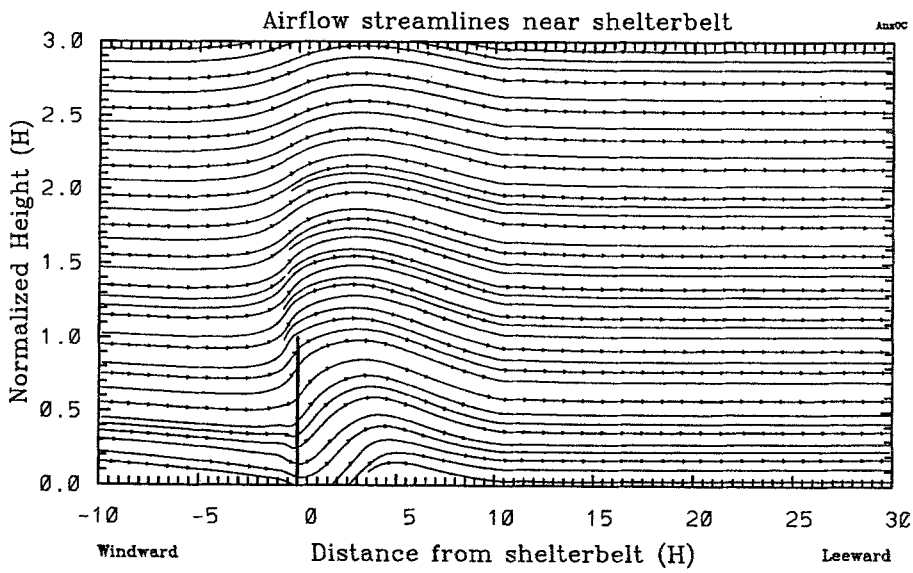

Fig. 1d. Same as Figure 1a but for a porosity of 0.40 ($k_r = 2.0$).

Perera (1981) made extensive measurements in the wind tunnel of different model fences with porosity ranging from 0.0 to 0.5. He showed that as the porosity of the fence increases, the recirculating bubble detaches from the fence and moves downstream. The recirculating bubble was detected for porosities of less than 0.3.

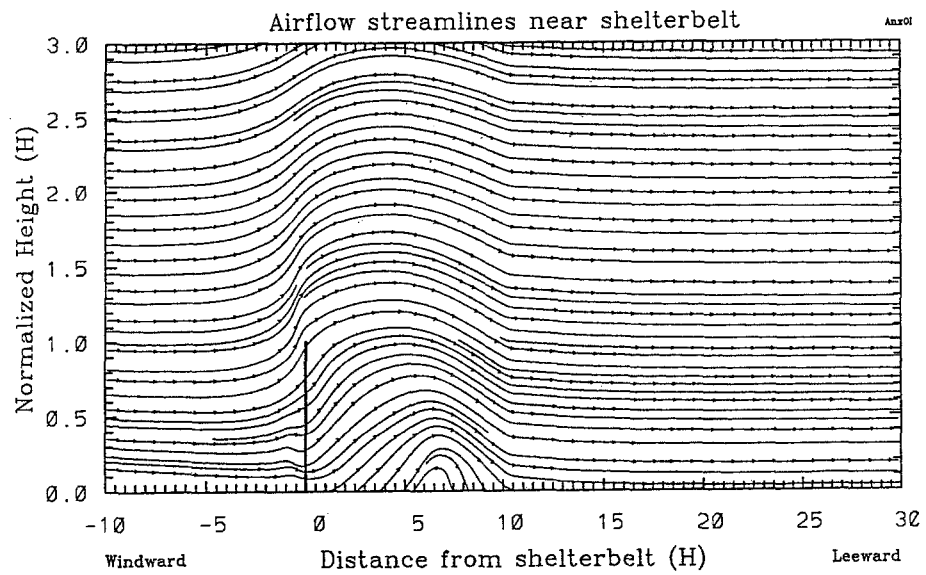

Fig. 1e. Same as Figure 1a but for a porosity of 0.30 ($k_r = 3.0$).

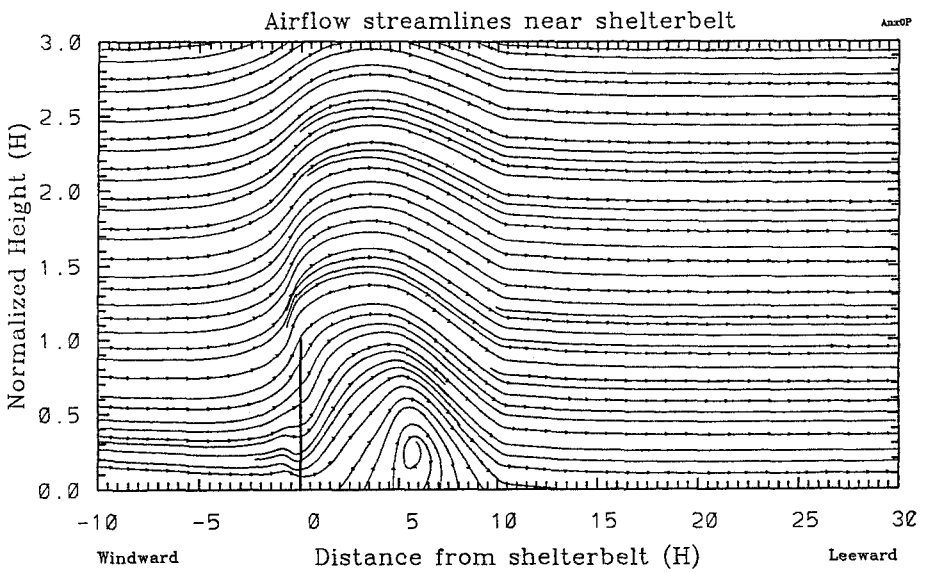

Fig. 1f. Same as Figure 1a but for a porosity of 0.27 ($k_r = 4.0$).

Castro's (1971) observations also support this conclusion. Therefore, our results agree with observed dependence of the recirculation point on porosity value.

The size of the separated recirculation increases with decreasing porosity. As shown in Table I, a small recirculating bubble develops near the ground far downstream of the shelterbelt with porosity of 0.3, and it enlarges and moves toward the

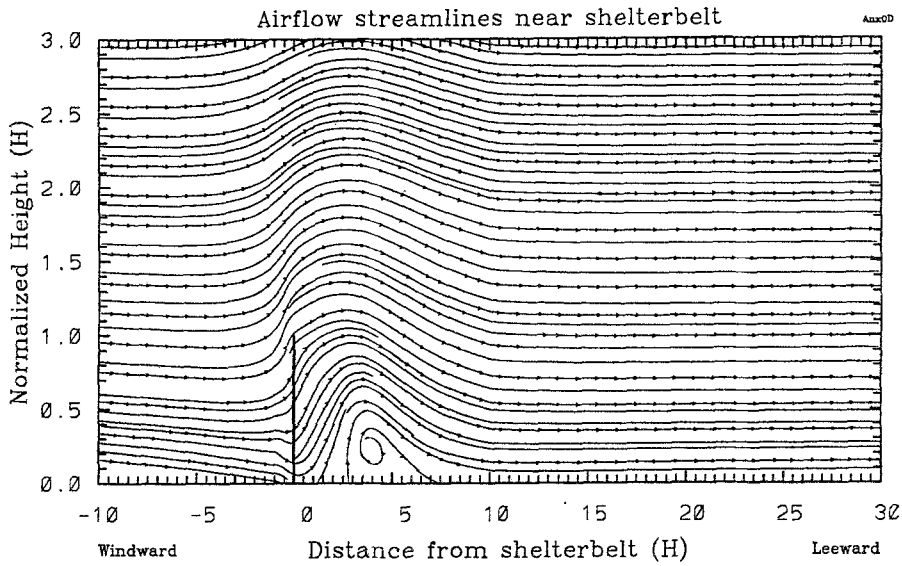

Fig. 1g. Same as Figure 1a but for a porosity of 0.25 (k_r = 4.5).

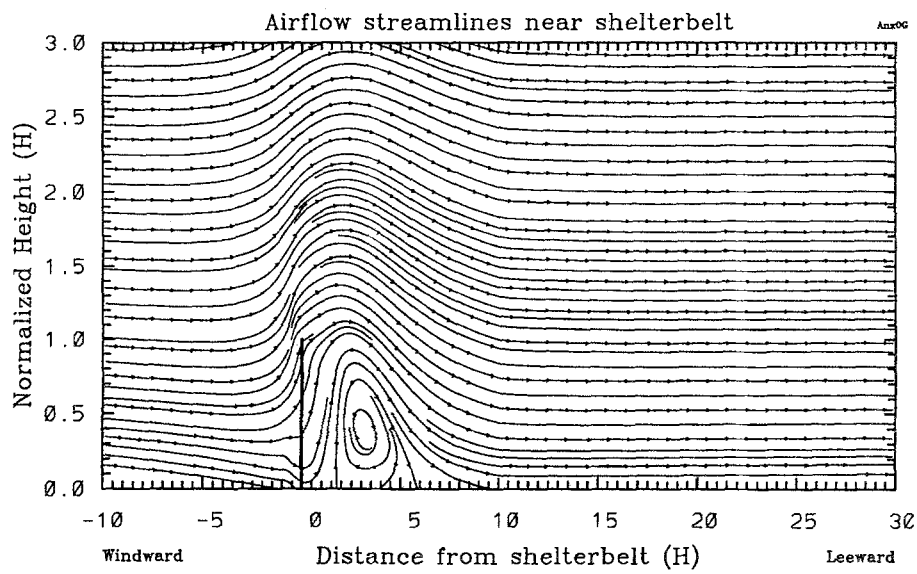

Fig. 1h. Same as Figure 1a but for a porosity of 0.14 (k_r = 18.0).

shelterbelt with decreasing porosity. The front and center move faster than the rear. The whole recirculating bubble ultimately develops a triangular zone bounded by a line from the top of the shelterbelt to a point on the ground between x=5 and 8 H from the shelterbelt.

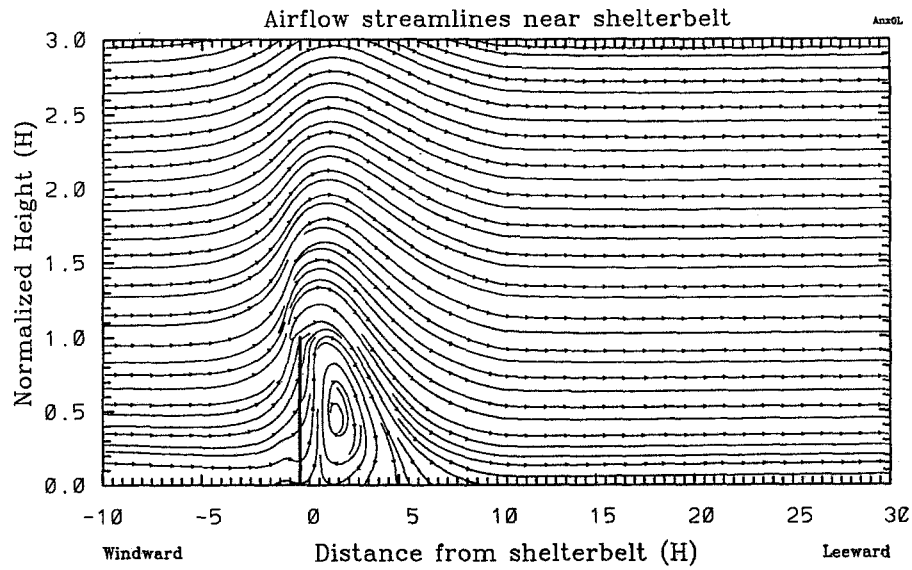

Fig. 1i. Same as Figure 1a but for a porosity of 0.08 (k_r = 60.5).

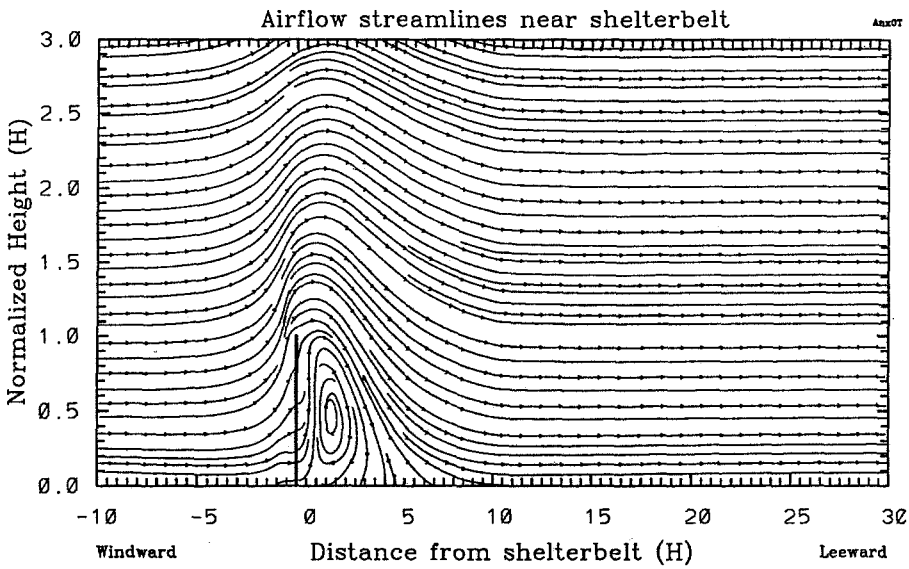

Fig. 1j. Same as Figure 1a but for a porosity of 0.06 (k_r = 128).

We now focus on specific characteristics of the flow patterns. A typical windspeed distribution for unseparated flow is shown in Figure 2a. The contour lines of windspeed show three ridges and a trough. The first ridge represents windspeed reduction immediately leeward and windward of a shelterbelt below shelterbelt height. The ridge line (i.e. the maximum windspeed reduction line) inclines

TABLE I

Change of recirculation bubble size with shelterbelt porosity (distances given in units of H)

Shelterbelt porosity	0.30	0.27	0.25	0.14	0.08	0.06
Bubble height (z)	0.20	0.50	0.60	0.80	0.90	1.00
Separation point (x)	5.00	4.00	2.50	1.50	0.75	0.00
Reattachment point (x)	8.00	7.50	6.50	6.00	5.50	5.00
Stagnation point (x)	6.50	5.50	4.00	3.25	2.00	1.00
(z)	0.15	0.25	0.30	0.35	0.40	0.50

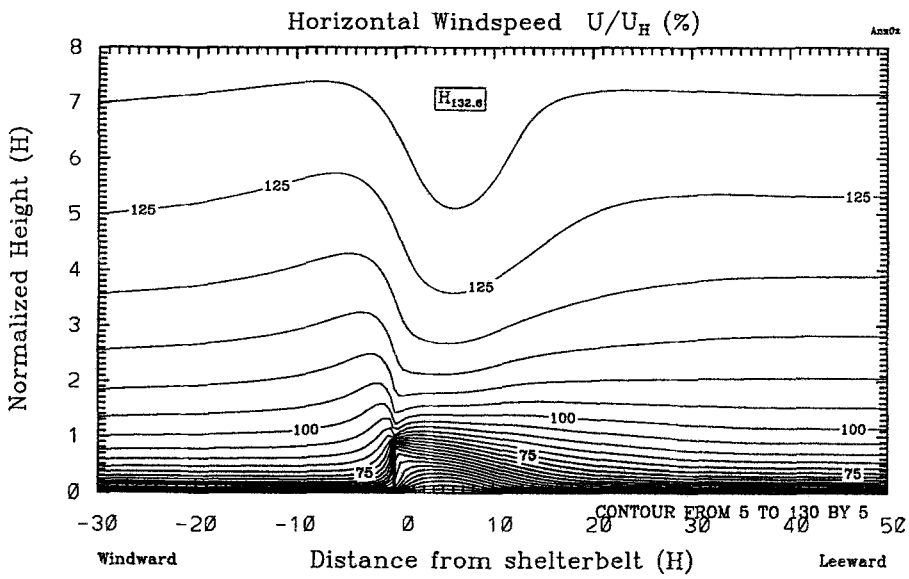

Fig. 2a. Windspeed field in the x–z plane near a shelberbelt with porosity of 0.4 (k_T = 2.0). The windspeed has been normalized by the upstream windspeed at the height H of the shelterbelt top. This is typical for unseparated flow (regime I).

upstream from about x = 4–5 H at ground level to x = 0 H at the top of the shelterbelt. This is the triangular-shaped sheltered zone of the shelterbelt (Plate, 1971; McNaughton, 1988). The second weak ridge is located above the top of the shelterbelt in the windward direction and results from the vertical transport of lower-level momentum in the shear flow. The third very weak ridge is due to the propagation of upstream divergence and convergence of windspeed. The trough is the speed-up zone over the shelterbelt required by mass continuity resulting from the pressure difference (discussed later). The trough line inclines downstream from the top of the shelterbelt.

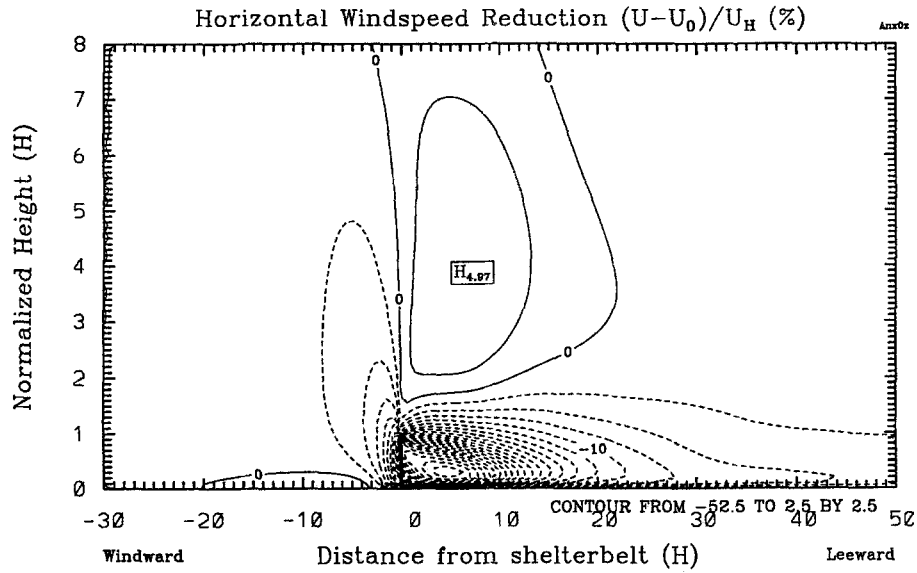

Fig. 2b. Same as Figure 2a except for windspeed reduction. The windspeed has been normalized by the upstream windspeed at the height H of the shelterbelt top.

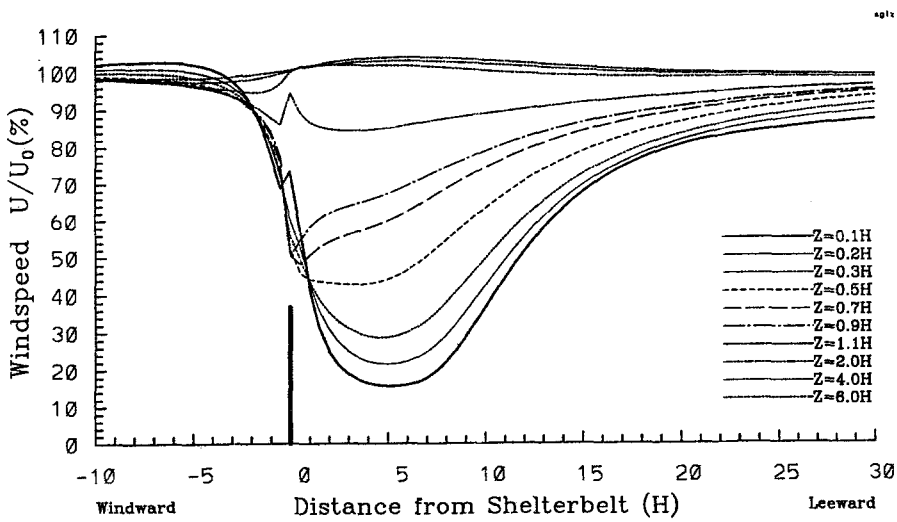

Fig. 2c. Horizontal distribution at various heights of windspeed normalized by the upstream windspeed at the same height for a shelterbelt with porosity of 0.4 (k_r = 2.0).

Shelter effects are more easily recognized from Figure 2b, which shows the difference between local windspeed and the upstream undisturbed windspeed at the same height normalized by the upstream windspeed at the height of the shelterbelt top. The shelterbelt generates three zones: a leeward windspeed-reduction zone, a windward windspeed-reduction zone and an overspeeding zone above the shelter-

belt. The maximum windspeed reduction is located about $x = 4$ H leeward and at a height of $z = 1/3$ H for homogeneous shelterbelts of intermediate density.

The shelter induces overspeeding above about 1.5 H as shown in Figure 2c. Below 1.5 H windspeed percentage shows a U-type distribution, with maximum windspeed reduction at about $x = 5$ H leeward at the $z = 0.1$ H level. The shelter effect, in terms of horizontal range where the windspeed is reduced at least 20%, is about 20 H in the lee. We also tested the sensitivity of the shelter distance to z_0/H, and the results are consistent with experimental and previous modeling studies (Van Eimern *et al.*, 1964; Wilson, 1985). In this paper, we use a z_0/H of 0.005 except in model verification where the measured z_0/H is used. With increasing height, the location of maximum windspeed reduction moves toward the shelterbelt, and the magnitude of the windspeed reduction rapidly diminishes. These simulated characteristics compare well with those indicated by Naegeli's data as shown in Figure 3 of van Eimern *et al.* (1964). This is typical for patterns of horizontal windspeed for unseparated flow.

Figures 3a–3g show characteristics of airflow patterns which are typical for separated flow. Figure 3a is the distribution of windspeed in the $x - z$ plane. Compared to Figure 2a (regime I), the basic three ridges and a trough also exist in regime II, but the steepness of contour lines obviously increases and a negative windspeed region forms in the lee. It should be noted that there is a region of relative mean calm (except for vertical flow) that surrounds the negative horizontal windspeed zone. For comparison with shelterbelt wind observations reported without regard to wind direction, the negative sign in the near lee should be ignored.

Separated flow (regime II) produces two windspeed-reduction maxima in the lee (Figure 3b) in contrast to a single center for unseparated flow (Figure 2b). While the reverse windspeed of the separated recirculation increases windspeed reduction near the ground, its return flow reduces windspeed reduction at higher levels (near 0.5 H) and forms these two centers. The reduction of absolute windspeed without regard to wind direction, which is perhaps more relevant for evaluating wind protection, is shown in Figure 3c. The distribution of reduction of absolute windspeed also has a center similar to that in regime I, but the center is located at $z = 0.85$ H, which is higher than the $z = 0.33$ H center of regime I. The reverse flow leads to higher windspeeds near the surface where the contour lines show a W-shaped distribution, thereby making the center of the maximum reduction of absolute windspeed much higher.

Figure 3d shows the distribution of absolute windspeed normalized by the upstream windspeed at the same height, which usually is considered as the descriptor of the sheltering effect. The minimum windspeed percentage (maximum shelter effect) has a λ-shaped distribution straddling a local maximum (caused by the recirculation) at the surface just beyond $x = 2$H, which is different from regime I where the minimum windspeed percentage is only a center near the ground.

The U-type distribution of windspeed percentage typical of regime I also occurs in regime II, but the maximum windspeed reduction is negative due to the reversed

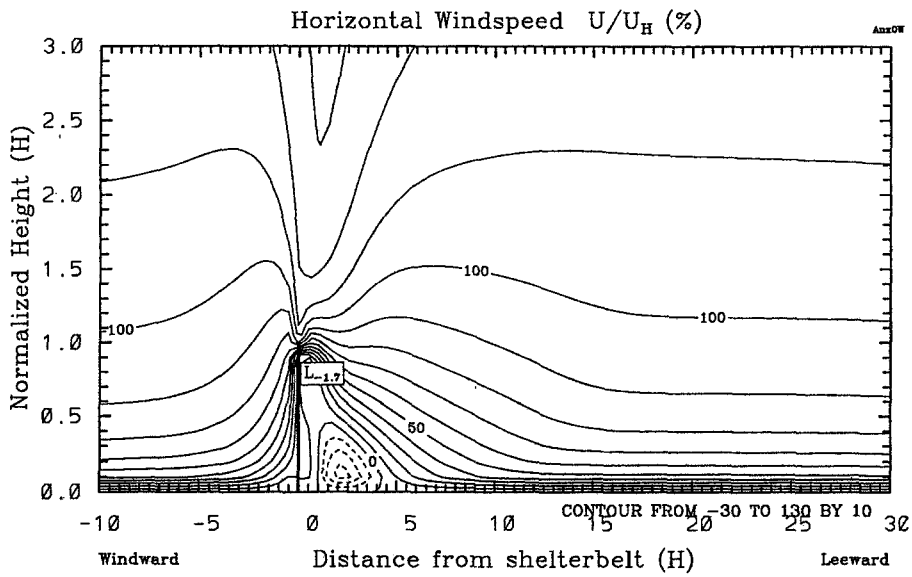

Fig. 3a. Windspeed field in the $x - z$ plane near the shelterbelt with porosity of 0.08 ($k_r = 60.5$). The windspeed has been normalized by the upstream windspeed at the height H of the shelterbelt top. This is typical for separated flow (regime II).

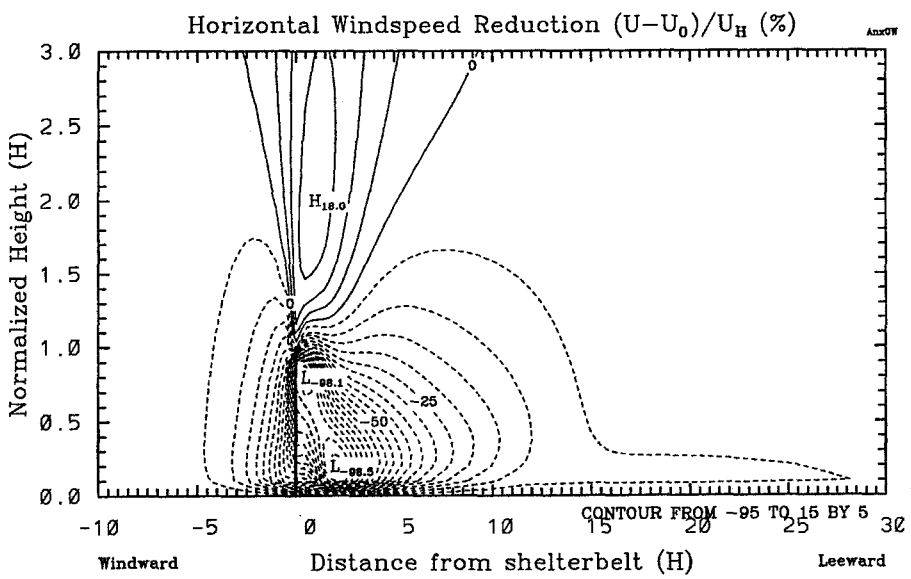

Fig. 3b. Normalized horizontal windspeed reduction for conditions of Figure 3a. The windspeed difference has been normalized by the upstream windspeed at the height H of the shelterbelt top.

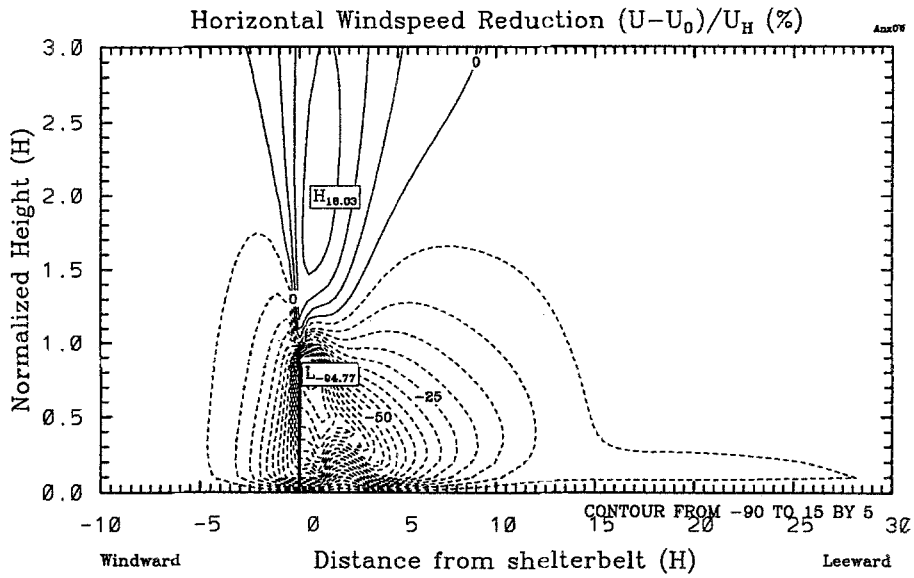

Fig. 3c. Same as Figure 3b except for the reduction of absolute windspeed.

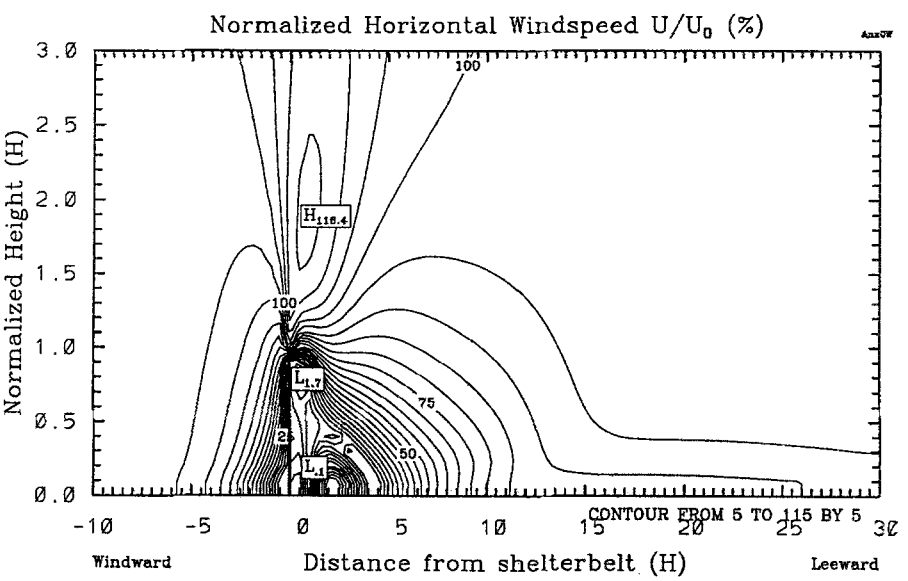

Fig. 3d. Same as Figure 3c except for the absolute value of windspeed normalized by the upstream windspeed at the same height.

wind of the recirculating bubble as shown in Figure 3e. In many practical applications, however, windspeed without regard to direction is of interest, so we have plotted the absolute windspeed percentage in Figure 3f. The reverse flow of regime

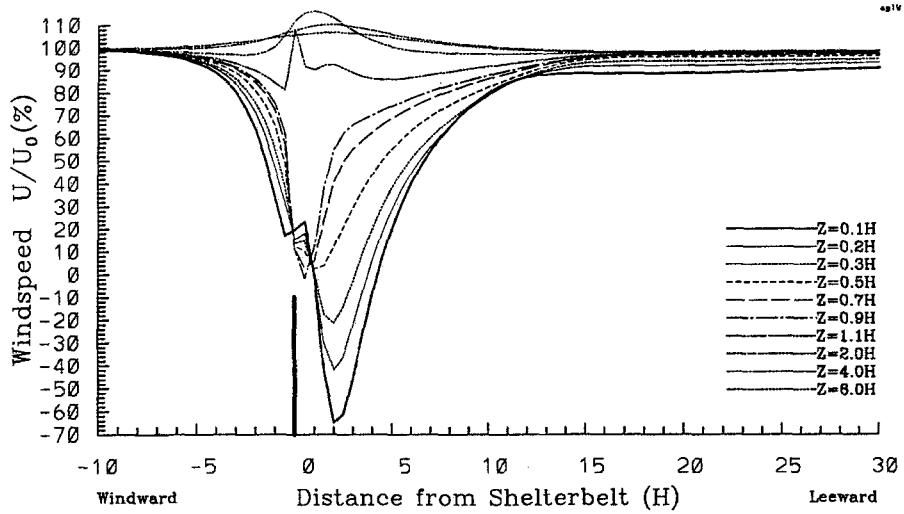

Fig. 3e. Horizontal distribution at various heights of windspeed normalized by the upstream windspeed at the same height for a shelterbelt with porosity of 0.08 (k_r = 60.5).

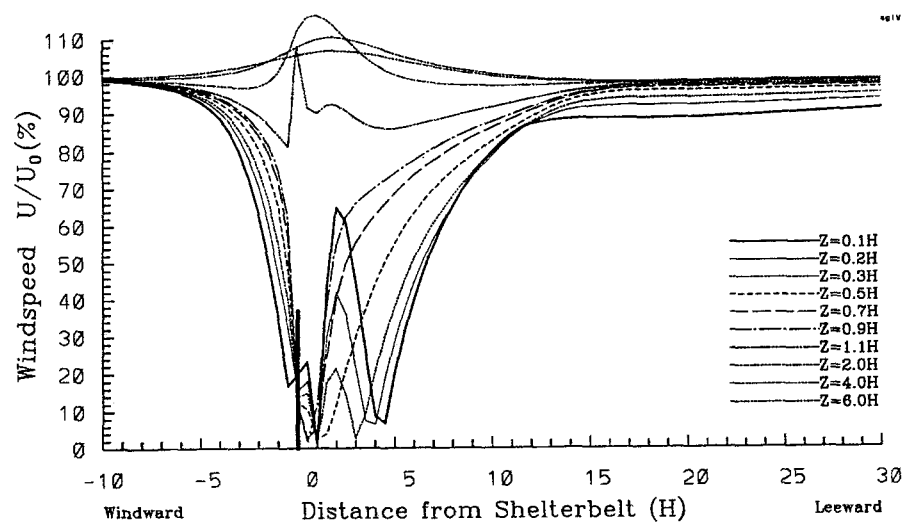

Fig. 3f. Same as Figure 3e except for horizontal distribution at various heights of the absolute value of windspeed normalized by the upstream windspeed at the same height.

II produces a W-type distribution which is different from regime I. Because the zone of near-calm winds between the shelter and the recirculating bubble (Figure 4e) is narrow, measurements by use of cup anemometers without accompanying direction sensors may lead to misinterpretation of the complexities of this flow field. The picture is further complicated because cup anemometers also respond partly to the turbulence. As shown in Figure 5 of van Eimern *et al.* (1964), the

recirculating bubble was observed in the wind tunnel, but does not appear in their Figures 2, 3 and 4. From Figures 2c and 3f, we can see that the change of windspeed reduction with height is smaller for a dense shelterbelt than for a medium-dense shelterbelt, especially within 10–20 H leeward where the shelter distance is determined by a critical windspeed reduction of 20%. This feature also can be identified from Naegeli's data as shown in Figure 3 of van Eimern *et al.* (1964). Therefore, with decreasing shelterbelt porosity, the sheltering effect, expressed in terms of the sheltered distance, is significantly reduced near the ground but only slightly reduced at higher levels.

From these results it is clear that field measurements made in the lee of shelters with porosity near or below the threshold for recirculation require very dense observations of speed and direction to capture details of the highly distorted flow. Since the reverse windspeed may be as large as 70% of the upstream windspeed at the same height, previous investigators may have treated the data of regime-II flows the same as regime-I flows, which may have led to a misinterpretation of some features of these flows. This may explain the contradictory conclusions in the literature about optimal sheltering porosity. Examples include Heisler and Dewalle's (1988) review paper, where their Figure 2b (data derived from Raine and Stevenson, 1977) shows a W-type distribution for an artificial barrier with porosity of 0 and their Figures 6, 7 and 8, where several points depart from the lines for smaller porosity. Also, in Figure 3 of van Eimern *et al.* (1964), the wavy structure of the horizontal profile of windspeed at $z = 0.25$ H departs from the patterns from higher levels and for higher permeability and could well be due to recirculation.

Wilson (1985) numerically simulated field observations for which the experimental results were described by Bradley and Mulhearn (1983) and Finnigan and Bradley (1983). We also have simulated these conditions and compare our results with both the experimental data and Wilson's (1985) results. The fence height (H = 1.2 m), resistance (pressure-loss) coefficient ($k_r = 2.0$), and roughness ($z_0 = 0.002$ m), used here are the measured values (Bradley and Mulhearn, 1983; Finnigan and Bradley, 1983), which are the same as those of Wilson (1985). We did not adjust these parameters.

Figure 4a presents the horizontal distribution of windspeed at heights of 0.4 H and 1.9 H, which were normalized by the upstream windspeed at height of 4 m. The observed data plotted in Figure 4a were taken from Figure 7 of Wilson (1985). The simulated results are in good agreement with observed data for both heights. Our model correctly predicts both the recovery rate and overspeeding.

We compare simulations of the vertical profile of wind with observations to further examine our prediction of the overspeeding zone. In Figure 4b, we plot the vertical profile of windspeed at $x = 4.2$ H normalized by windspeed at the 4-m height. The observed data were taken from Figure 4 of Wilson (1985). Our simulation agrees well with observed overspeeding above 1.5 H.

Wilson (1985) used several models to simulate these flow fields, but his simulated windspeed recovery rates were slower than the data indicate. Alternatively,

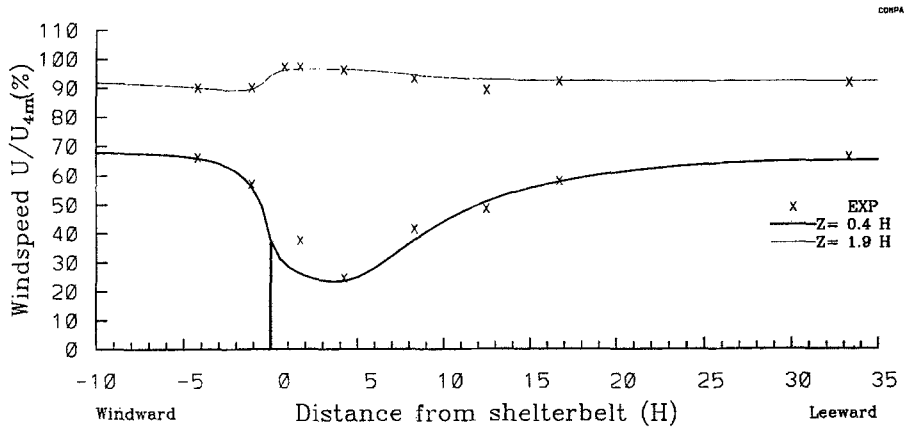

Fig. 4a. Comparisons of simulated and observed horizontal profiles of windspeed at $z = 0.4$ H and $z = 1.9$ H. The windspeed was normalized by the upstream windspeed at $z = 4$ m. The observed data were taken from Wilson (1985).

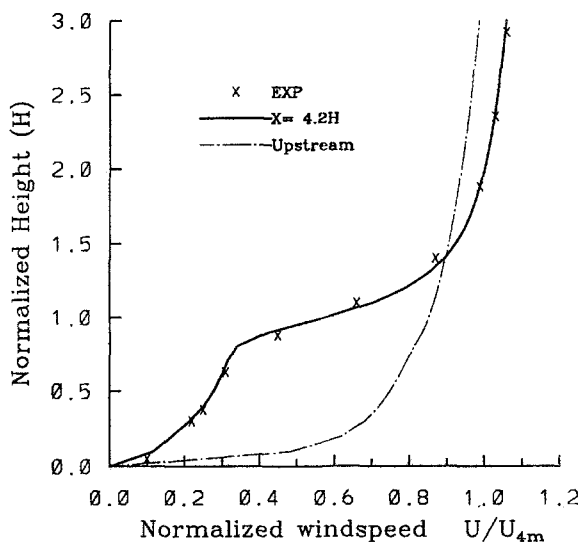

Fig. 4b. Comparison of simulated and observed vertical profiles of windspeed at $x = 4.2$ H. The windspeed was normalized by the upstream windspeed at $z = 4$ m. The vertical profile of undisturbed upstream windspeed is also plotted. The observed data were taken from Wilson (1985).

the windspeed recovery distance is longer than the data suggest. If we define the sheltered distance to be the downwind point where at $z = 0.4$ H the wind recovers to 60% of the 4 m-height windspeed, the data indicate a shelter distance of 18 H. However, Wilson's prediction in his Figure 7 is larger than 30 H. These results suggest his simulations underpredicted windspeed in the speed-up zone and overpredicted that length of the sheltered zone.

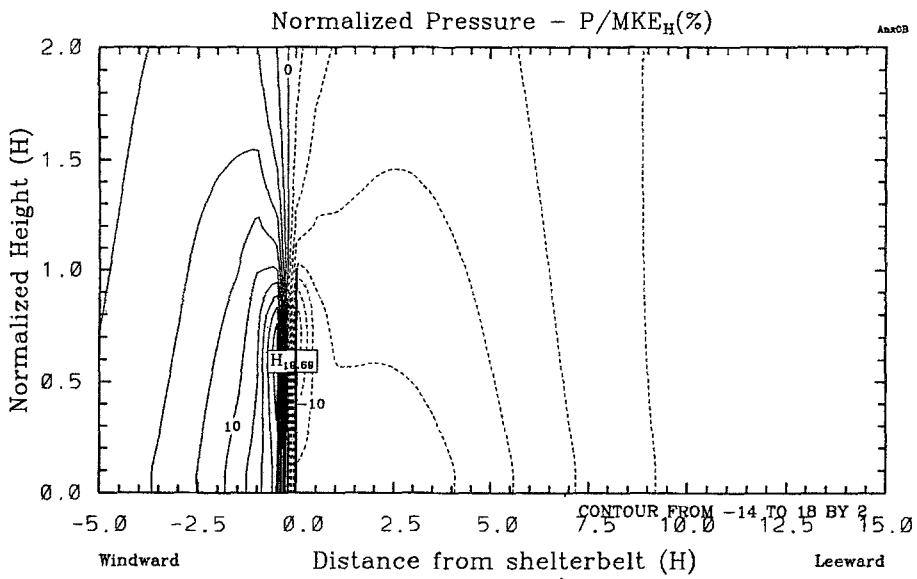

Fig. 5a. Distribution of perturbed pressure field near the shelterbelt with porosity of 0.62 ($k_T = 0.5$). The pressure perturbation was normalized by the upstream mean kinetic energy (MKE) at height H of the shelterbelt top.

From a comparison of our results with those of Wilson (1985), we conclude that past interpretations of shelterbelt flow fields, based on turbulent diffusion theory, may have overemphasized the role of turbulent diffusion in the formation of leeward flows. We find that interaction between the disturbed pressure and the flow is also an important mechanism for creating the sheltering effect. The pressure gradient on the windward side is much larger than leeward, as shown in Figure 5. In the first several H leeward, the pressure gradient is very small and is related to the porosity of the shelterbelt. The other important characteristic which affects the windspeed-recovery rate is the zone of larger pressure gradient beyond the leeward zone of weak pressure gradient. Measurements of pressure along the ground behind a solid obstacle have shown that the negative pressure downstream of the obstacle is approximately constant over a distance of about 3 H and then starts rising very rapidly (Chang, 1966; Plate, 1971).

The pressure perturbation arises when air passing through the shelterbelt experiences a drag force that creates a static pressure difference. The pressure perturbation extends beyond the shelterbelt, forming a pressure gradient that opposes the flow and causes windspeed reductions both leeward and windward. The leeward pressure gradient causes the point of maximum windspeed reduction to locate far from the shelterbelt (e.g. 2–6 H) and sets up horizontal convergence in the near lee and divergence downwind of this point. The convergence and divergence of the flow fields create positive dynamic pressure in the near lee and negative dynamic pressure in the far lee. Therefore, between the shelter and the point of maximum windspeed

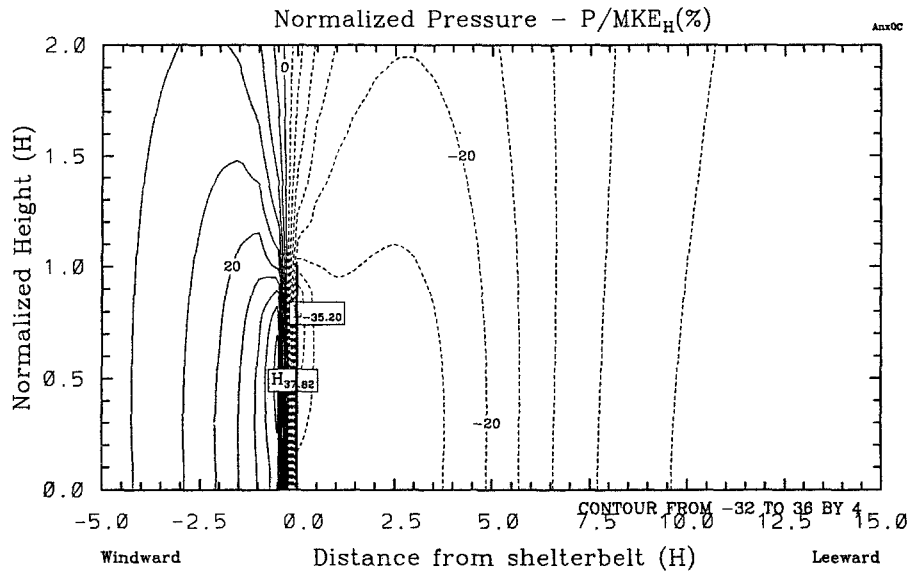

Fig. 5b. Same as Figure 5a but for a porosity of 0.4 (k_r = 2.0).

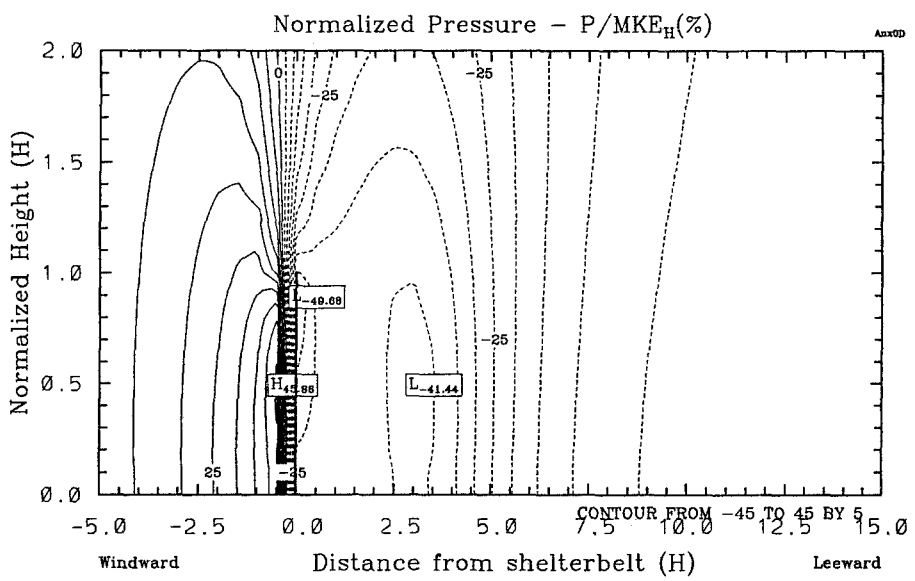

Fig. 5c. Same as Figure 5a but for a porosity ol 0.25 (k_r = 4.5).

reduction, a second maximum negative-pressure-perturbation center may occur when dynamic pressure is large and the static-pressure perturbation is weak (Figure 5c). But leeward of the point of maximum windspeed reduction, the negative dynamic-pressure perturbation produces a large pressure-gradient zone.

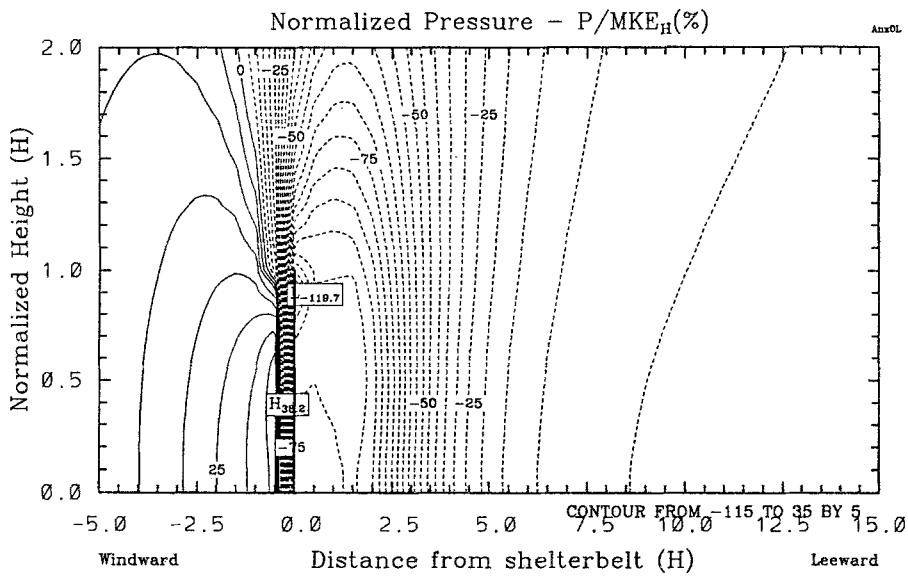

Fig. 5d. Same as Figure 5a but for a porosity of 0.08 (k_r = 60.5).

In shear flow, the transport of horizontal momentum by vertical velocity also may result in a dynamic-pressure perturbation. Strong upward flow windward of the shelter transports air with a momentum deficit from lower to higher levels, resulting in flow convergence and a positive dynamic-pressure perturbation. In the lee, downward flow generates a negative dynamic-pressure perturbation. The convergence of windspeed upwind of the shelterbelt also generates positive dynamic pressure. These effects lead to the overspeeding phenomenon that we simulate above the shelterbelt.

Interaction of the dynamic pressure with the flow produces additional pressure that moves the location of the leeward maximum windspeed reduction away from the shelterbelt and makes the windspeed recovery toward its upstream undisturbed value more rapid. The dynamic pressure gradients exist in both horizontal and vertical directions. The difference between ground and free stream pressure tends to compress the streamlines toward the ground. These effects lead to the faster recovery rate of windspeed (compared to Wilson, 1985) that we simulate in the lee.

We experimented with several turbulent closure schemes and observed that different turbulent schemes produce some difference in the predicted value of TKE. However, mean flow is insensitive to different turbulent closure schemes, which is consistent with Wilson's (1985) findings, and the effect of the shelterbelt on turbulence is determined, to some degree, by the modification of the mean flow field. TKE distributions around shelterbelts with different densities are shown in Figures 6a–d, where TKE was normalized by the undisturbed upstream TKE at the same

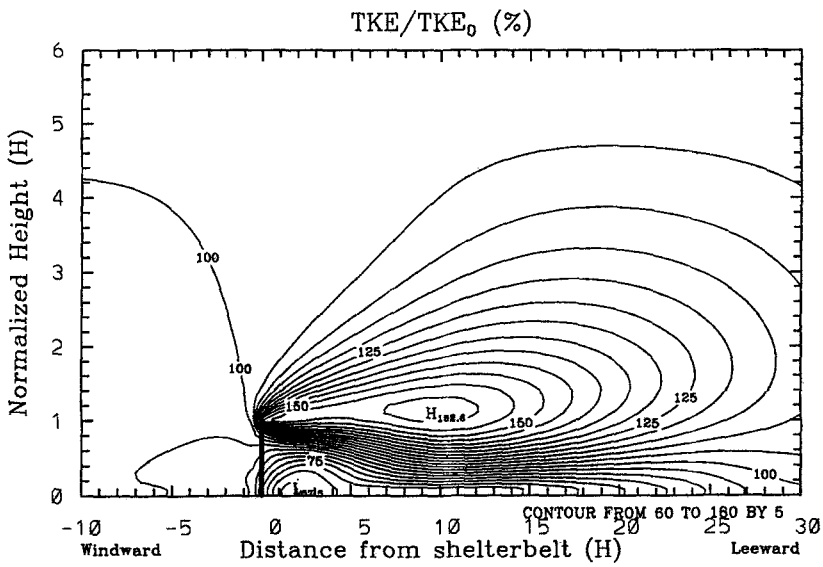

Fig. 6a. Distribution of turbulent kinetic energy (TKE) near the shelterbelt with porosity of 0.62 (k_r = 0.5). The TKE was normalized by the undisturbed upstream TKE at the same level.

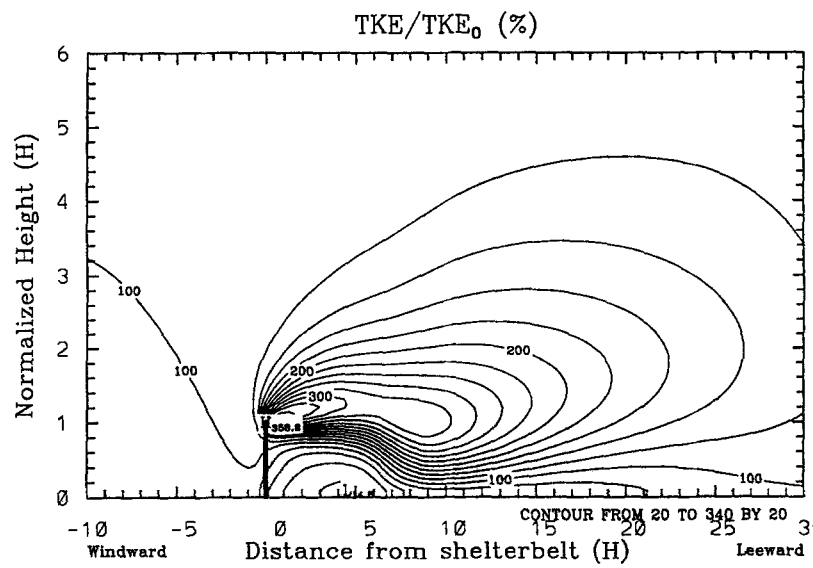

Fig. 6b. Same as Figure 6a but for a porosity of 0.4 (k_r = 2.0).

level (TKE_0) to minimize the effects of both turbulent closure schemes and windspeed. These four figures show two common characteristics: a strong turbulence zone at the top of the shelterbelt and a weak turbulence zone near the ground. This is consistent with experimental findings as summarized by McNaughton (1988): there exists a triangular quiet zone of reduced turbulence and smaller eddy sizes

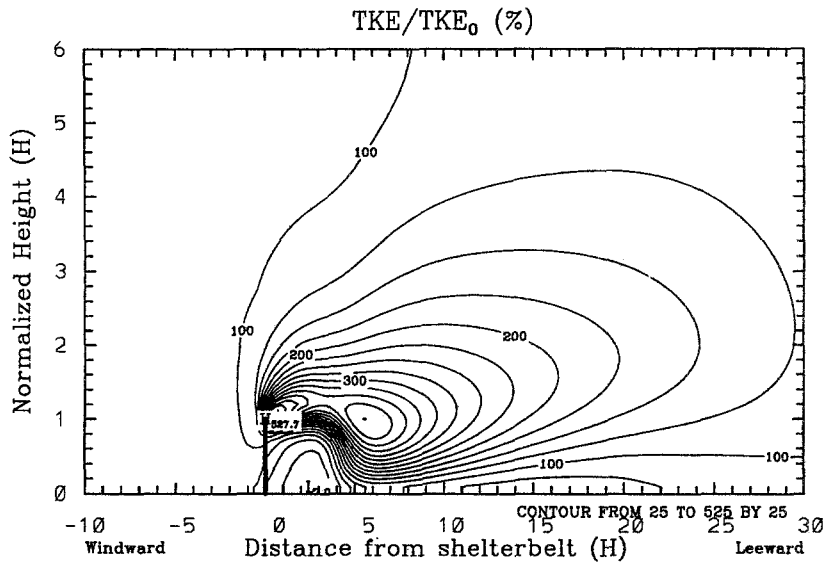

Fig. 6c. Same as Figure 6a but for a porosity of 0.20 (k_r = 8.0).

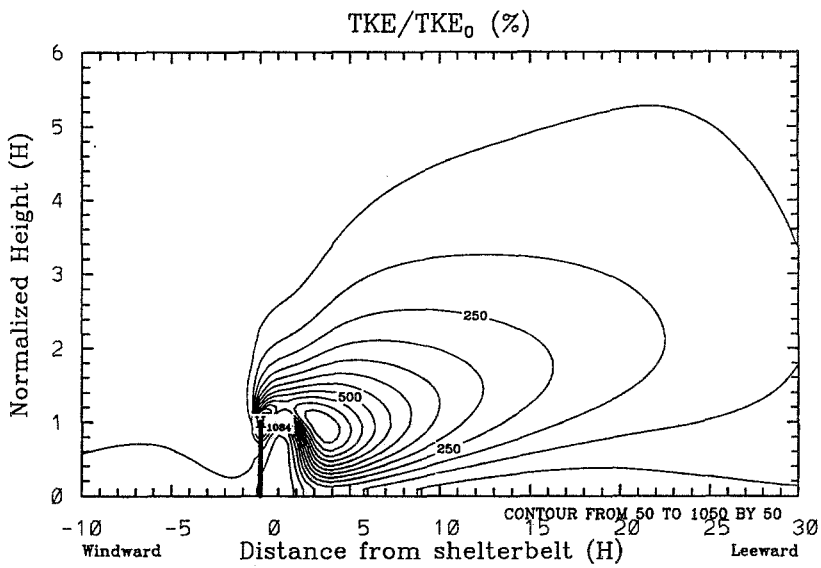

Fig. 6d. Same as Figure 6a but for a porosity of 0.06 (k_r = 128).

immediately behind the shelterbelt and beneath the strong wake turbulence zone. As shown in Figures 6a–6d, the shapes of the triangular quiet zone and the wake zone change with shelterbelt density. For a porosity of 0.62, the strong turbulence center of the wake zone is at x = 10 H and z = 1 H. However, the wake zone has two centers for shelterbelts with porosity less than 0.4. One center is immediately

at the shelterbelt top. The other is 3–9 H downstream, and shifts toward the shelter with increasing shelterbelt density, moving from $x = 9$ H and $z = 1$ H for porosity of 0.4 to $x = 3$ H and $z = 0.9$ H for porosity of 0.06. Therefore, the size of the quiet zone decreases with increasing shelterbelt density. For a dense shelterbelt with porosity of 0.06 (Figure 6d), the quiet zone is limited to a horizontal distance of 2 H immediately behind the shelter, and the region from 2 to 9 H leeward has larger TKE than in the undisturbed flow. This may explain why Plate (1972) reported higher evaporation rates behind a solid screen than behind a porous one. A dense shelterbelt also decreases turbulence immediately behind it, as shown within 2 H leeward from the shelterbelt in Figure 6d. Perera (1981) also reported that a solid fence provides a flow of very low turbulence in the zone close to the shelter.

5. Conclusion

We have used a numerical model to build a complete set of shelterbelt flow patterns and describe their changes with porosity. The location of maximum windspeed reduction, its changes with porosity, and the leeward windspeed recovery rate are all well simulated. The separated recirculation and the changes of its size and location with porosity are also well simulated, and the critical porosity leading to separation agrees with the observed value of 0.3. The simulated characteristics of shelter aerodynamics qualitatively agree with field observations and laboratory wind-tunnel measurements. Quantitative comparisons with observed data and the simulations of Wilson (1985) show that our model gives correct predictions of both the windspeed-recovery rate in the lee and overspeeding over the shelterbelt. The model demonstrated good performance for flows over and through shelters ranging from almost completely open, where the governing equations are parabolic, to almost solid shelterbelts, where the governing equations are elliptic and where separated flow exists.

We studied the patterns and dynamic processes of flows over and through shelterbelts as determined by the structure or porosity of shelterbelts and demonstrate the importance of dynamic pressure in determining wind-sheltering functions and characteristics. The interaction of penetrating flow with the perturbation pressure and flows over the shelter creates a point of maximum windspeed reduction far behind the shelterbelt. The dynamic pressure resulting from convergence and divergence of the flow field alters the perturbation pressure field. The disturbed pressure controls not only the formation of the separated flow but also the location of maximum windspeed reduction, streamline curvature, speed-up over the shelterbelt, and leeward windspeed-recovery rate. The interaction of pressure and flows produces complex flow patterns, the characteristics of which are determined, to a great extent, by the ratio of the penetrating flow to undisturbed flow, or permeability. The permeability is controlled by shelterbelt structure, which traditionally is expressed in terms of porosity or leaf-area index density.

Although the leeward windspeed-reduction zone is most important for practical applications, all parts of the flow pattern are interconnected. Overspeeding over the shelterbelt alters streamline curvature and hence affects windspeed-recovery rate. The windward windspeed reduction affects the overspeeding zone by changing the drag force and vertical transport of horizontal momentum.

We have tested our model on shelters with a spectrum of densities ranging from nearly open to nearly solid. The resulting flow patterns can be divided into two regimes depending on whether the flow separates. It seems that the maximum shelter effects exist in the transient state between regime I (unseparated flow) and regime II (separated flow). Therefore, only when the theoretical and numerical model has good performance between parabolic-type equations when shelterbelt density is low and elliptic-equations when shelterbelt density is high, can we conclude that accurate simulation of all regimes of the flow-field evolution near shelterbelts is possible.

6. Acknowledgement

We are grateful for the very critical and helpful review of an early draft of this manuscript by R. W. Arritt. We also thank the anonymous referee for very helpful suggestions. This research was supported by USDA/CSRS NRI Competitive Grant #93371018954.

References

Baines, W. D. and Peterson, E. G.: 1951, 'An Investigation of Flow Through Screens', *Trans . Am. Soc. Mech. Eng.* **73**, 467–480.

Bradley, E. F. and Mulhearn, P. J.: 1983, 'Development of Velocity and Shear Stress Distributions in the Wake of a Porous Shelter Fence', *J. Wind Eng. Ind. Aerodyn.* **15**, 145–156.

Caborn, J. M.: 1957, 'Shelterbelts and Microclimate', *For. Comm. Bull.* No. 29, Edinburgh, 129 pp.

Castro, I. P.: 1971, 'Wake Characteristics of Two-Dimensional Perforated Plates Normal to an Airstream', *J. Fluid Mech.* **46**, 599–609.

Chang, S. C.: 1966, 'Velocity Distributions in the Separated Flow behind a Wedge-shaped Model Hill', Thesis, Colorado State University, Ft. Collins, CO, 101 pp.

Chorin, A. J.: 1968, 'Numerical Solution of the Navier–Stokes Equations', *Math. Comp.* **23**, 341–354.

Counihan, J., Hunt, J. C. R., and Jackson, P. S.: 1974, 'Wakes Behind Two-Dimensional Surface Obstacles in Turbulent Boundary Layers', *J. Fluid Mech.* **64**, 529–563.

Finnigan, J. J.: 1985, 'Turbulent Transport in Flexible Plant Canopies', in B. A. Hutchison and B. B. Hicks (eds.), *The Forest- Atmosphere Interaction*, D. Reidel Publishing Company, Boston, pp. 443–480.

Finnigan, J. J. and Bradley, E. F.: 1983, 'The Turbulent Kinetic Energy Budget Behind a Porous Barrier: an Analysis in Streamline Coordinates', *J. Wind. Eng. Ind. Aerodyn.* **15**, 145–156.

Hagen, L. J. and Skidmore, E. L.: 1971, 'Turbulent Velocity Fluctuations and Vertical Flow as Affected by Windbreak Porosity', *Trans. ASAE* **14**, 634–637.

Hagen, L. J., Skidmore, E. L., Miller, P. L., and Kipp, J. E.: 1981, 'Simulation of Effect of Wind Barriers on Airflow', *Trans. ASAE* **24**, 1002–1008.

Heisler, G. M. and Dewalle, D. R.: 1988, 'Effects of Windbreak Structure on Wind Flow', *Agriculture, Ecosystems and Environment* **22/23**, 41–69.

Hoerner, S. F.: 1965, 'Fluid Dynamic Drag', Library of Congress Catalog Card Number 64-19666.
Jensen, M.: 1974, 'The Aerodynamics of Shelter'. In: *FAO Report on the FAO/DANIDA Inter-regional Training Center on Heathland and Sand Dune Afforestation*. FAO/DEN/TF, 123 pp.
Kaiser, H.: 1959, 'Die Stromung an Windschutzstreifen', *Ber. Deut. Wetterdienstes* **7**, 36 pp.
Li, Z., Lin, J. D., and Miller, D. R.: 1989, 'Air Flow Over and Through a Forest Edge: A Steady-State Numerical Simulation', *Boundary-Layer Meteorol.* **46**, 333–354.
McNaughton, K. G.: 1988, 'Effects of Windbreaks on Turbulent Transport and Microclimate', *Agriculture, Ecosystems and Environment* **22/23**, 17–39.
Mellor, G. L. and Yamada, T.: 1974, 'A Hierarchy of Turbulence Closure Models for Planetary Boundary Layers', *J. Atmos. Sci.* **31**, 1791–1806.
Mellor, G. L. and Yamada, T.: 1982, 'Development of a Turbulent Closure Model for Geophysical Fluid Problems', *Rev. Geophys. Space Sci.* **20**, 851–875.
Meyers, T. and Paw U, K. T.: 1986, 'Testing of A Higher-Order Closure Model for Modeling Airflow Within and Above Plant Canopies', *Boundary-Layer Meteorol.* **37**, 297–311.
Miller, D. R., Lin, J. D., and Lu, Z. N.: 1991, 'Air Flow Across an Alpine Forest Clearing: A Model and Field Measurements', *Agricultural and Forest Meteorol.* **56**, 209–225.
Naot, O. and Mahrer, Y.: 1991, 'Two-Dimensional Microclimate Distribution Within and Above a Crop Canopy in an Arid Environment: Modeling and Observational Studies', *Boundary-Layer Meteorol.* **56**, 223–244.
Paegle, J., Zdunkowski, W. G., and Welch, R. M.: 1976, 'Implicit Differencing of Predictive Equations of the Boundary Layer', *Mon. Wea. Rev.* **104**, 1321–1324.
Perera, M. D. A. S.: 1981, 'Shelter Behind Two-Dimensional Solid and Porous Fences', *J. Wind Eng. Ind. Aerodyn.* **8**, 93–104.
Plate, E. J.: 1971, 'The Aerodynamics of Shelterbelts', *Agricultural Meteorol.* **8**, 203–222.
Raine, J. K. and Stevenson, D. C.: 1977, 'Wind Protection by Model Fences in a Simulated Atmospheric Boundary Layer', *J. Indust. Aerodyn.* **2**, 159–180.
Raupach, M. R. and Shaw, R. H.: 1982, 'Averaging Procedures for Flow Within Vegetation Canopies', *Boundary-Layer Meteorol.* **22**, 79–90.
Richards, P. J., Kay, E. F., Russell, D., and Wilson, G. R. C.: 1984, 'Porous Artificial Windbreaks in Oblique Winds', *Paper 67/84 for IPENZ Conf.*, Hastings, New Zealand, 10 pp.
Rosenberg, N. J.: 1979, 'Windbreaks for Reducing Moisture Stress', in B. J. Barfield and J. F. Gerber (eds.), *Modification of Aerial Environment of Plants*, ASAE, St Joseph, pp. 538.
Sturrock, J. W.: 1969, 'Aerodynamics Studies of Shelterbelts in Nealand-1: Low to Medium Height Shelterbelts in Mid-Canterbury', *N. Z. J. Sci.* **12**, 754–776.
Sturrock, J. W.: 1972, 'Aerodynamics Studies of Shelterbelts in Nealand-2: Medium Height to Tall Shelterbelts in Mid-Canterbury', *N. Z. J. Sci.* **15**, 113–140.
Taylor, P. A.: 1988, 'Turbulent Wakes in the Atmospheric Boundary Layer', in W. L. Steffen and O. T. Denmead (eds.), *Flow and Transport in the Natural Environment: Advances and Applications*, Springer-Verlag, Berlin, pp. 270–292.
Thom, A.S.: 1975, 'Momentum, Mass and Heat Exchange of Plant Communities', *Vegetation and the Atmosphere*, Vol. 1, Academic Press, pp. 1–278.
van Eimern, J., Karschon, R., Razumova, L. A., and Robertson, G. W.: 1964, 'Windbreaks and Shelterbelts', World Meteorol. Org. Technical Note No. 59, pp. 188.
Wang, H., and Takle, E. S.: 1995, 'Boundary-Layer Flow and Turbulence Near Porous Obstacles. I. Derivation of a General Equation Set for a Porous Medium', *Boundary-Layer Meteorol.* (in press).
Whitaker, S.: 1968, *Introduction to Fluid Mechanics*, Prentice-Hall, Englewood Cliffs.
Whitaker, S.: 1969, 'Advances in Theory of Fluid Motions in Porous Media', *Ind. Eng. Chem.* **61**, 14–28.
Whitaker, S.: 1973, 'The Transport Equations for a Multi-phase System', *Chem. Eng. Sci.* **28**, 139–147.
Wilson, N. R. and Shaw, R. H.: 1977, 'A Higher Order Closure Model for Canopy Flow', *J. Applied Meteorol.* **16**, 1197–1205.
Wilson, J. D.: 1985, 'Numerical Studies of Flow Through a Windbreak', *J. Wind Eng. Ind. Aerodyn.* **21**, 119–154.

Wilson, J. D.: 1987, 'On the Choice of a Windbreak Porosity Profile', *Boundary-Layer Meteorol.* **38**, 37–39.

Wilson, J. D.: 1988, 'A Second-Order Closure Model for Flow Through Vegetation', *Boundary-Layer Meteorol.* **42**, 371–392.

Yamada, T.: 1982, 'A Numerical Model Study of Turbulent Airflow in and above a Forest Canopy', *J. Meteorol. Soc. Japan* **60**, 438–454.

Yamada, T. and Mellor, G. L.: 1975, 'A Simulation of the Wangara Atmospheric Boundary Layer Data', *J. Atmos. Sci.* **32**, 2309–2329.